

Numerical Simulation of a Catastrophe Model for Coronal Mass Ejections

T. G. FORBES

Institute for the Study of Earth, Oceans, and Space, University of New Hampshire, Durham

In 1978, W. Van Tend and M. Kuperus proposed a simple catastrophe model for magnetically driving coronal mass ejections, prominence eruptions, and two-ribbon flares. Their model, which is based on simple circuit concepts, suggests that a stable configuration containing a current filament will lose equilibrium when the filament current exceeds a critical value. Here we use a two-dimensional numerical simulation to test how the Van Tend–Kuperus model works in an ideal MHD fluid. The simulation exhibits the expected loss of mechanical equilibrium near the predicted critical value, but the current filament moves only a short distance upward before coming to rest at a new equilibrium. However, this new equilibrium contains a current sheet which is resistively unstable to magnetic reconnection, and if magnetic reconnection occurs rapidly, the filament can continue to move upward at Alfvénic speeds.

1. INTRODUCTION

Since the early observations of coronal mass ejections (CMEs) by OSO 7 and Skylab [Tousey, 1973; Gosling *et al.*, 1974], three different forces have been considered for driving CMEs, namely, (1) the magnetic force due to coronal currents [e.g., Anzer, 1978; Mouschovias and Poland, 1978; Pneuman, 1984; Linker *et al.*, 1990], (2) the pressure force due to the thermal energy generated by a flare [e.g., Wu *et al.*, 1978; Steinolfson *et al.*, 1978], and (3) the gravitational force due to the buoyancy of a preexisting structure [e.g., Low, 1981]. Although buoyancy may play some role in initiating a mass ejection, it is unlikely to be the main driving force, since the gravitational potential energy of the preexisting structure is estimated to be much less than the 10^{32} ergs needed for a large CME [Wagner *et al.*, 1981; Yeh, 1985]. Thus most models are based on a pressure mechanism, a magnetic mechanism, or a combination of the two.

Pressure mechanisms due to heating of the corona plasma by a flare have become unpopular during the last few years, primarily for two reasons. First, most CMEs are associated with prominence eruptions rather than flares [Kahler, 1987], and second, a flare associated with a CME typically begins several minutes after the CME has already started [Wagner, 1982; Simnett and Harrison, 1985]. Therefore it is difficult to think of a CME as simply a consequence of flare activity. It seems more likely that the flare is a chromospheric manifestation of the large-scale magnetic disruption which drives both the CME and the flare. Accordingly, there is now a renewed interest in magnetically driven models of CMEs [see Hundhausen, 1988; Steinolfson, 1989].

While there have been many numerical simulations of pressure-driven models for CMEs [e.g., Wu *et al.*, 1978; Steinolfson, 1988], there have been relatively few simulations of magnetically driven models. They are more difficult to simulate because the distribution of currents and fields in the corona prior to a CME are not well known. Plausible configurations which have been suggested include twisted magnetic loops [e.g., Hood and Priest, 1979; Van Hoven, 1981], sheared arcades [e.g., Birn and Schindler, 1981; Zwingmann, 1987; Aly, 1985; Mikic *et al.*, 1988; Biskamp

and Welter, 1989], line currents [e.g., Van Tend and Kuperus, 1978; Sturrock, 1987; Démoulin and Priest, 1988; Steele and Priest, 1990], plasmoids [Pneuman, 1984; Linker *et al.*, 1990], and various arrangements of current sheets [e.g., Shibata *et al.*, 1989; Forbes, 1988].

The numerical simulations in this paper are based on a line current configuration proposed by Van Tend and Kuperus [1978] and Van Tend [1979] and subsequently developed as a circuit model by Kaastra [1985] and Martens and Kuin [1989] and as an MHD model by van Ballegooijen and Martens [1989] and Priest and Forbes [1990]. Figure 1 shows the magnetic field for two equilibrium states of this configuration, which is everywhere potential except for an infinitely thin line current at the center of a magnetic island. These two states have the same vertical magnetic field component at $y = 0$, and they are equilibria because the combined magnetic field from all the current sources external to the filament is zero at the location of the filament. As we will see later, the state having only an o-type neutral line (Figure 1a) is stable, while the state having both o-type and x-type neutral lines (Figure 1b) is unstable (cf. section 2).

The magnetic field configurations of Figure 1 are due to three separate current elements consisting of a line current at a height h above the x axis, an image line current at a depth $-h$ below the x axis, and a two-dimensional dipole at a depth $-d$ below the x axis. The dipole alone determines the normal magnetic field component B_y at the photospheric boundary, and as long as the dipole strength and position are kept constant, the photospheric field lines remained fixed in position (i.e., line-tied).

In general, equilibria occur only if the relative dipole strength is greater than a certain critical value, and if the relative strength is less than this critical value there are no equilibria. Consequently, a CME, a flare, or a prominence eruption can be modeled by allowing the photospheric background field, represented by the dipole, to slowly decrease below the critical value. Alternatively, one can increase the strength of the filament current to accomplish the same result.

The next section presents a two-dimensional “vacuum model” based on the configuration shown in Figure 1. This vacuum model treats the current filament as a perfectly conducting wire, the photosphere as a perfectly conducting plate, and the region surrounding the wire as a vacuum.

Copyright 1990 by the American Geophysical Union.

Paper number 90JA00457.
0148-0227/90/90JA-00457\$05.00

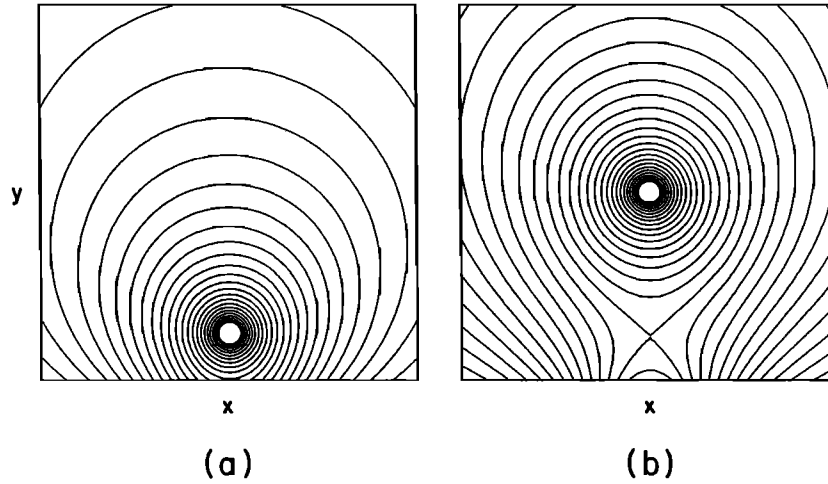


Fig. 1. Contours of constant magnetic potential for the two equilibrium states of the vacuum model.

Since the electrical resistivity of the vacuum is infinite, magnetic reconnection at the x line below the filament is completely uninhibited, and a current sheet cannot form at the x line.

The MHD simulation in this study uses the magnetic field configuration of the vacuum model as an initial condition, and a principal goal is to determine to what extent predictions based on the vacuum model are valid. Thus the simulation should not be thought of as a quantitative model of a solar CME, but rather as a numerical experiment of a mechanism for driving CMEs.

2. VACUUM MODEL PROTOTYPE

Figure 1 shows the magnetic field configuration of the vacuum model for two equilibrium states having the same normal magnetic field at the photosphere. In each configuration there is a filament of radius r located at a height h above the photosphere, and the magnetic field outside the filament is

$$B_y + iB_x = i(\mu/2\pi) \left[\frac{2hI}{z^2 + h^2} + \frac{m}{(z + id)^2} \right] \quad (1)$$

where $z = x + iy$ is the complex coordinate, μ is the magnetic permeability of free space, I is the filament current, and m is the strength of a dipole moment located at depth $-d$ below the x axis. The Dirichlet boundary condition for the normal field component along the base is

$$B_y(x, 0) = (\mu/\pi)mx/(x^2 + d^2)^2 \quad (2)$$

In the limit of zero radius the field (1) is equivalent to the combined field from a line current at $y = h$, an image line current at $y = -h$, and a two-dimensional dipole of strength m at $y = -d$. The image line current repels the current filament, and the dipole attracts it. But repulsion and attraction are balanced when

$$h/d = M - 1 \pm (M^2 - 2M)^{1/2} \quad (3)$$

where

$$M = m/Id \quad (4)$$

is a dimensionless parameter which gives the relative strength between the dipole and the filament current. Figure 2 plots the filament locations which are equilibria. For $M < 2$, there are no equilibria, and if M slowly decreases with time, a dynamic catastrophe will occur when M falls below 2. The catastrophe manifests itself as the upward ejection of the filament toward a new equilibrium at $h = \infty$.

The reason for choosing a two-dimensional dipole to represent the photospheric background field is that it is the simplest boundary condition which gives a background field that falls off with height faster than $1/y$. Van Tend [1979] found that if the background field falls off with height as $1/y$ or slower, no catastrophe occurs. Instead, as M decreases, the equilibrium height h increases without any sudden tran-

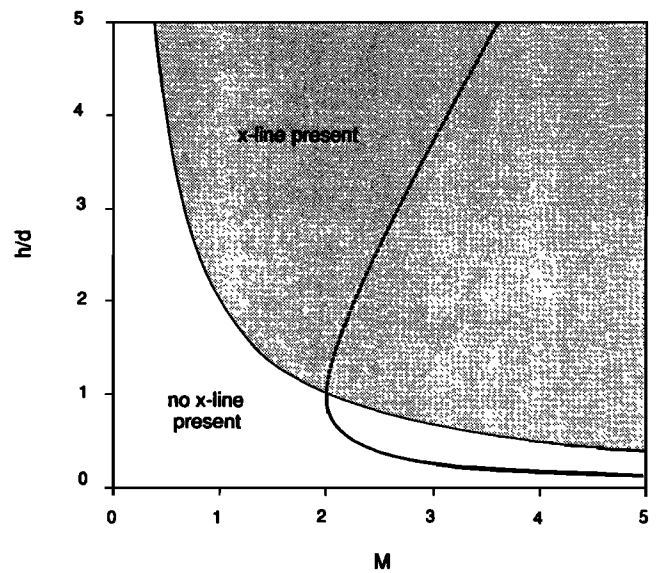


Fig. 2. The location of vacuum equilibria when the radius of the current filament is zero. The quantities h , d , and M are the height of the filament, the depth of the photospheric dipole, and the relative strength of the dipole, respectively. The dashed and solid portions of the curve indicate the unstable and stable equilibria, respectively, and the shaded region indicates the regime where an x line is present in the magnetic field.

sition or catastrophe. Thus in a two-dimensional multipole expansion of the boundary field the dipole term is the first term which gives an equilibrium curve with a built-in catastrophe.

In order to determine the stability of the equilibria it is necessary to know how the filament current changes when the filament is moved upward or downward. If there is no external electrical generator in the circuit containing the filament, then Lenz's law requires the magnetic flux enclosed by the circuit to be constant [cf. *Reitz and Milford*, 1960, p. 171]. In the two-dimensional vacuum model the circuit consists of the filament current and a return surface current at $y = 0$. Thus for a filament of radius r the flux in the circuit is

$$\begin{aligned}\phi &= \int_0^{h-r} B_x(0, y) dy \\ &= (\mu/2\pi) \left[I \ln \left(\frac{2h}{r} - 1 \right) - \frac{m}{d} \frac{h-r}{h-r+d} \right] \quad (5)\end{aligned}$$

and as the filament's height varies, the current I varies so as to keep ϕ constant. For small r , (5) gives a filament current which decreases with increasing h as

$$I = I_0 \left[1 - \frac{\ln(h/h_0)}{\ln(h_0/r)} \right] \quad (6)$$

where I_0 and h_0 are the initial current and location of the filament. In the limit that the filament radius r tends to zero, the decrease in I also tends to zero. The decrease in I becomes infinitesimally small in this limit, because the flux between the filament and the boundary becomes infinite as r tends to zero. Consequently, an infinitesimal decrease in the filament current suffices to keep the flux constant.

In general, the force on the filament per unit length is

$$F = \iint_S j(B_x - B_y) dx dy \quad (7)$$

where S is the area of the filament. If the radius of the filament is small, then the integral in (7) is approximately $IB_x(0, h)$ to second order in the expansion parameter $r/(2h)$. Thus to second order, the force per unit length is

$$F = \frac{\mu}{\pi} I \left[\frac{I}{4h} - \frac{m}{2(h+d)^2} \right] \quad (8)$$

and from (5)

$$I = \frac{m}{d} \left\{ \frac{2f + (h-r)/(h-r+d)}{\ln[(2h/r) - 1]} \right\} \quad (9)$$

where

$$f \equiv \frac{\pi d}{\mu m} \phi \quad (10)$$

is a dimensionless measure of the flux ϕ .

The change in magnetic energy that occurs when the filament moves is given by the magnetic work:

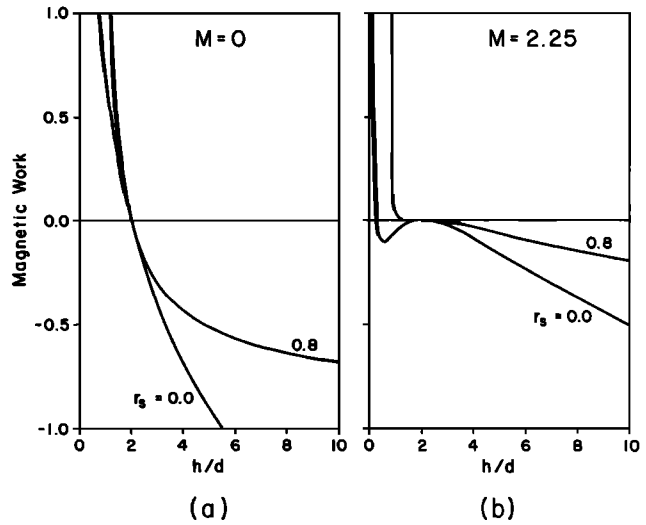


Fig. 3. Magnetic work in units of $\mu I_0^2/(4\pi d)$ as a function of filament height h/d . A background field does not exist in Figure 3a but does in Figure 3b. The quantity r_s is the filament radius in units of d .

$$W_b = - \int_{h_0}^h F(h') dh' \quad (11)$$

Substituting (8) and (9) into (11) and numerically integrating gives the results shown in Figure 3. For all of the curves shown the initial starting location h_0 is set at $2d$, and the initial energy is set to zero. In the limit of $r = 0$, (11) can be integrated analytically to give

$$W_b = \left(\frac{\mu I_0^2}{4\pi} \right) \left[-\ln \left(\frac{h}{2d} \right) + \frac{2M}{3} \left(\frac{h-2d}{h+d} \right) \right] \quad (12)$$

where M is defined with respect to the initial filament current as $m/I_0 d$. For $r = 0$ an infinite amount of magnetic energy is released as the filament moves out toward $h = \infty$, but for $r > 0$ the energy release is finite.

The minimum and the maximum of the $r = 0$ curve in Figure 3b correspond to the stable and unstable branches of the equilibrium curve of Figure 2. The shape of the energy curves makes the equilibria in the upper branch of Figure 2 unstable and the equilibria in the lower branch stable.

In general, for $r > 0$ the location of an equilibrium depends not only upon M but also upon the initial location of the filament. If initially the filament is not in equilibrium, then the location of its equilibria are prescribed not by (3) but instead by the relation

$$f = \frac{hd \ln[(2h/r) - 1]}{(h+d)^2} - \frac{h-r}{2(h-r+d)} \quad (13)$$

where f is the flux parameter defined by (10). Plotting h/d as a function of f gives equilibrium curves which are independent of the initial starting position of the filament as shown in Figure 4. All of the equilibrium curves for $r > 0$ terminate at $f = 0$ when the surface of the current filament touches the base boundary.

For $r > 0$ the stability of the equilibria is determined by the sign of the derivative dF/dh of the force given by (8) and (9). The force is stabilizing for the lower branch of the equilib-

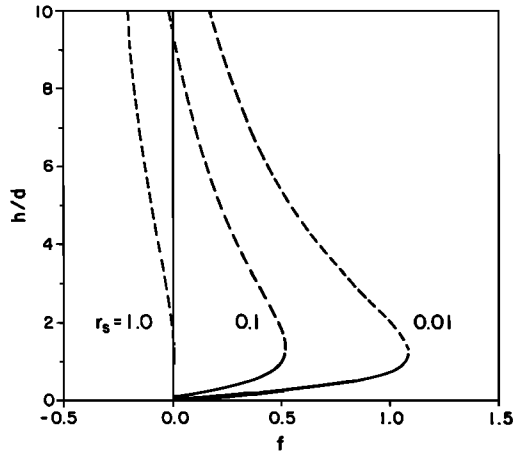


Fig. 4. The location of vacuum equilibria when the radius of the current filament is greater than zero. The quantity f is the flux between the photosphere and the lower edge of the filament, while the quantity r_s is the filament radius in units of d .

rium curve shown in Figure 4 but destabilizing for the upper branch.

3. MHD SIMULATION

Let us now consider what happens if the filament and the vacuum surrounding it are replaced by an ideal MHD fluid. To analyze this MHD system, we use a time-dependent two-dimensional numerical simulation that solves an initial-boundary-value problem within a rectangular domain.

3.1. Mathematical Formulation

The system of differential equations for the simulation are

$$\partial \mathbf{B} / \partial t = -\nabla \times (\mathbf{v} \times \mathbf{B}) \quad (14)$$

$$\partial \rho / \partial t = -\nabla \cdot (\rho \mathbf{v}) \quad (15)$$

$$\rho [\partial \mathbf{v} / \partial t + (\mathbf{v} \cdot \nabla) \mathbf{v}] = -\nabla p + \mathbf{j} \times \mathbf{B} \quad (16)$$

$$\partial p / \partial t + (\mathbf{v} \cdot \nabla) p = -\gamma p (\nabla \cdot \mathbf{v}) \quad (17)$$

$$\mathbf{j} = \nabla \times \mathbf{B} \quad (18)$$

$$p = \rho T \quad (19)$$

where \mathbf{B} , \mathbf{v} , ρ , and p are the dimensionless magnetic field, velocity, density, and pressure defined by

$$\rho = \rho' / \rho_c' \quad p = p' / (\gamma R' \rho_c' T_c') \quad c_s'^2 = \gamma R' T_c'$$

$$\mathbf{B} = \mathbf{B}' / c_s' (\rho_c' \mu')^{1/2} \quad \mathbf{v} = \mathbf{v}' / c_s'$$

From this point on, a prime superscript indicates a dimensional quantity, while the absence of a prime superscript indicates a dimensionless quantity. The normalizing parameters ρ_c' , ρ_c' , T_c' , and c_s' are the ambient coronal values of the density, pressure, temperature, and sound speed, respectively. The constant μ' is the magnetic permeability of free space, γ is the ratio of specific heats, and R' is the universal gas constant. The magnetic field \mathbf{B}' is normalized so that at $|\mathbf{B}| = 1$ the Alfvén speed $v_A' (= B_c' / (\mu' \rho_c')^{1/2})$ equals the sound speed c_s' .

The dimensionless space and time coordinates, x , y , and t , are defined by

$$x = x' / w' \quad y = y' / w' \quad t = t' c_s' / w'$$

where w' is an arbitrary scale length. Here we choose w' equal to the width of the simulation domain, such that $0 < x < 1$ and $0 < y < 2$. This choice of w' means that a sound wave in the ambient medium takes unit time to travel from the axis of symmetry to the side boundary. The corresponding dimensionless current density is

$$j = \mu' w' j' / B_c'$$

and the dimensionless temperature is given by (19).

The initial conditions for the six independent variables, B_x , B_y , v_x , v_y , p , and ρ , are

$$B_x = B_\phi(R_-)(y - h_0)/R_- - B_\phi(R_+)(y + h_0)/R_+ - B_\phi(r + \Delta/2)Md(r + \Delta/2)[x^2 - (y + d)^2]/R_d^4 \quad (20)$$

$$B_y = -B_\phi(R_-)x/R_- + B_\phi(R_+)x/R_+ - B_\phi(r + \Delta/2)Md(r + \Delta/2)2x(y + d)/R_d^4 \quad (21)$$

$$v_x = 0 \quad (22)$$

$$v_y = 0 \quad (23)$$

$$p = p_0 - \int_{R_-}^{\infty} B_\phi(R)j(R) dR \quad (24)$$

$$\rho = \rho_0(p/p_0)^{1/\gamma} \quad (25)$$

where

$$B_\phi(R) = -\frac{j_0}{2} R \quad 0 \leq R \leq r - \Delta/2 \quad (26a)$$

$$B_\phi(R) = -\frac{j_0}{2R} \left\{ \frac{1}{2} (r - \Delta/2)^2 - (\Delta/\pi)^2 + \frac{1}{2} R^2 + (\Delta R/\pi) \sin [\pi(R - r + \Delta/2)/\Delta] + (\Delta/\pi)^2 \cos [\pi(R - r + \Delta/2)/\Delta] \right\} \quad (26b)$$

$$r - \Delta/2 < R < r + \Delta/2$$

$$B_\phi(R) = -\frac{j_0}{2R} [r^2 + (\Delta/2)^2 - 2(\Delta/\pi)^2] \quad (26c)$$

$$r + \Delta/2 \leq R < \infty$$

$$j(R) = j_0 \quad 0 \leq R \leq r - \Delta/2 \quad (27a)$$

$$j(R) = j_0 \frac{1}{2} \{ \cos [\pi(R - r + \Delta/2)/\Delta] + 1 \} \quad (27b)$$

$$r - \Delta/2 < R < r + \Delta/2$$

$$j(R) = 0 \quad r + \Delta/2 \leq R < \infty \quad (27c)$$

and

$$R_\pm^2 = x^2 + (y \pm h_0)^2 \quad (28)$$

$$R_d^2 = x^2 + (y + d)^2 \quad (29)$$

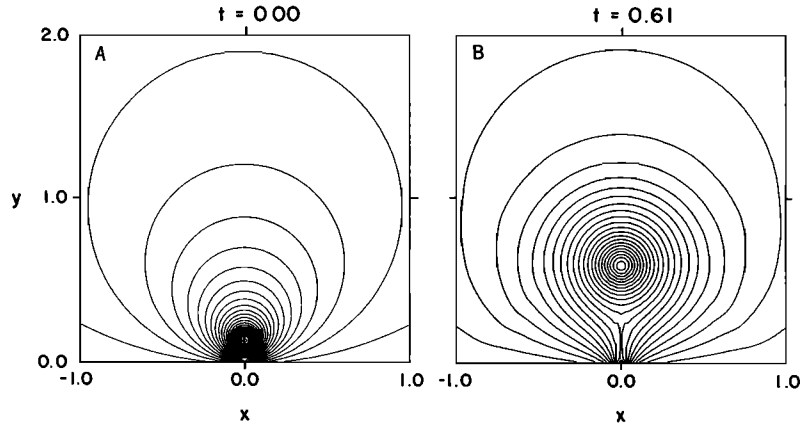


Fig. 5. Contours of constant vector potential for the nonequilibrium case with a photospheric dipole strength of $M = 1.0$ (case 3). The time t is in units of the acoustic scale time of the numerical box.

The initial magnetic field configuration prescribed by (20) and (21) is shown in Figure 5a. The functions $B_\phi(R)$ and $j(R)$ give the field and current density of an isolated filament as a function of radial distance R . From the center of the filament to $r - \Delta/2$ the current density is j_0 , while from $r + \Delta/2$ to ∞ the current density is 0. Between $r - \Delta/2$ and $r + \Delta/2$ the current density decreases such that at $R = r$ the current density is $j_0/2$. The initial pressure prescribed by (24) balances the magnetic pressure and tension within the current filament only when the image and background fields are absent. Thus the initial state inside the filament is never in precise equilibrium. Condition (26) for the initial density comes from arbitrarily assuming that the initial entropy is uniform.

For the numerical simulation we set $r = 0.05$, $\Delta = 0.025$, $h_0 = 0.125$, $j_0 = 600$, $p_0 = 1/\gamma$, $\rho_0 = 1$, and $\gamma = 5/3$. The value of 0.05 for r gives a filament radius of just 2.5 times the grid resolution of $\Delta x \approx 0.02$, so the internal structure of the filament is not well resolved. However, using such a small radius makes the box scale length much larger than the filament scale length, and this prevents the open boundary conditions from influencing the early evolution of the filament. The values for p_0 and ρ_0 give a dimensionless sound speed of unity at infinity, while the value for j_0 gives a magnetic field strength such that the minimum plasma β is about 0.1.

Different values of the parameters d and M were chosen, as shown in Table 1. Of the 12 cases shown in the table, two correspond to stable equilibria in the vacuum model (cases

11 and 12), one corresponds to an unstable equilibrium in the vacuum model (case 7), and the rest correspond to nonequilibria in the vacuum model (cases 1–6 and cases 8–10).

Since the filament magnetic field falls off as $1/r$, the plasma β tends to ∞ at large distances from the filament. Consequently, the plasma β in the numerical simulation is >100 at the top of the box (cf. Figure 6). In reality the plasma β of the ambient corona always remains less than unity, since the pressure decreases rapidly with height due to gravity stratification. However, in the simulation the pressure is constant with height, since gravity is not yet included.

Boundary conditions are as follows: Along $x = 0$, symmetry conditions are used, while along $y = 2$ and $x = 1$, open conditions are used that set the normal derivatives of \mathbf{v} , p , ρ , and the tangential component of \mathbf{B} to zero (see Forbes [1988] for details). Along $y = 0$ the independent boundary conditions are

$$j = 0 \quad (30)$$

$$v_x(x, 0, t) = 0 \quad (31)$$

$$v_y(x, 0, t) = 0 \quad (32)$$

and the compatibility relations (i.e., dependent boundary conditions) are

$$B_y(x, 0, t) = B_y(x, 0, 0) \quad (33)$$

$$\left. \frac{\partial p(x, y, t)}{\partial y} \right|_{y=0} = 0 \quad (34)$$

TABLE 1. Parameters for Numerical Cases

Case	M	d	h_0/d	r/d	f
1	0.0	0.0625	2.0	0.8	∞
2	0.5	0.0625	2.0	0.8	1.1136
3	1.0	0.0625	2.0	0.8	0.4204
4	1.5	0.0625	2.0	0.8	0.1894
5	2.0	0.0625	2.0	0.8	0.0738
6	2.125	0.0625	2.0	0.8	0.0535
7	2.25	0.0625	2.0	0.8	0.0353
8	2.5	0.0625	2.0	0.8	0.0045
9	2.75	0.0625	2.0	0.8	-0.0207
10	3.0	0.0625	2.0	0.8	-0.0417
11	2.25	0.25	0.5	0.2	0.1619
12	3.125	0.5	0.25	0.1	0.0411

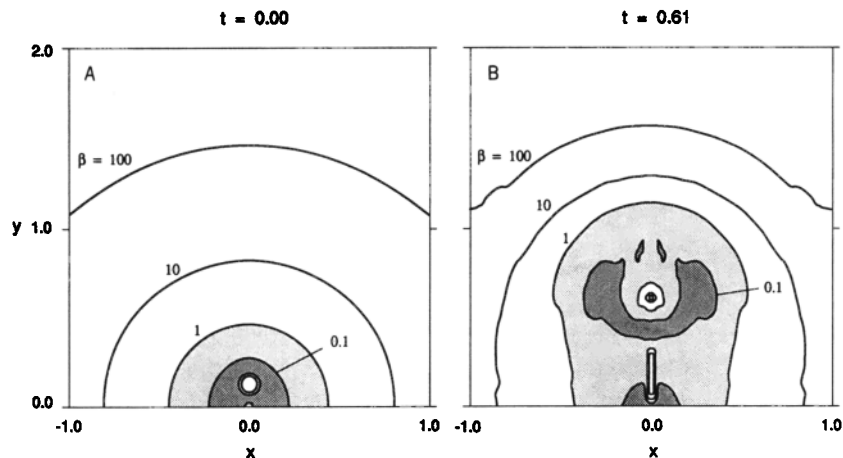


Fig. 6. Contours of constant plasma β for case 3 at $t = 0$ and $t = 0.61$. Dark shading denotes $0.1 > \beta > 0.01$, and light shading denotes $1.0 > \beta > 0.1$. The unusually large values of β at the top of the box are due to the lack of a gravitationally stratified medium.

$$\rho(x, 0, t) = p(x, 0, t)^{1/\gamma} \quad (35)$$

Conditions (30) and (31) are both dissipative boundary conditions which produce a numerically unresolved Hartmann layer at the base. The first of these two conditions is the no-slip condition for a viscous fluid, while the second is the line-tying condition for an ohmic fluid. These nonideal conditions are used here because they are considerably easier to implement than the equivalent ideal conditions [Forbes and Priest, 1987]. Unlike the nonideal conditions the ideal conditions have compatibility relations which can be expressed only as differential equations, and these differential equations must be solved numerically at each point along the boundary at each time step [Wu and Wang, 1987]. By using the dissipative boundary conditions we avoid this complication but at the cost of introducing an unresolved boundary layer at the base. Condition (32) is the wall condition which together with (30) and (31) and the initial conditions (22), (23), and (25) gives the compatibility relations (33)–(35) [Forbes, 1988].

The MHD system of equations (14)–(18) is solved by using the explicit, flux-corrected transport code SHASTA (sharp and smooth transport algorithm) developed by Boris and Book [1973, 1976] and Weber *et al.* [1979]. SHASTA is well suited for studying shock waves, since it can sustain a sharp shock transition over only two or three mesh points. Furthermore, shock transitions in SHASTA are free of spurious oscillations caused by the Gibbs' phenomenon. SHASTA solves the equations in a conservative form so that quantities such as mass, momentum, magnetic flux, and total energy are normally conserved to high accuracy (<1% error). Large errors are sometimes generated in the pressure and temperature if the plasma β is greatly different from unity, but these errors can be reduced if the conservative form of the energy equation is replaced by an energy equation for the pressure. Since the β varies from 0.1 to >100 in our simulation, we have used an energy equation for the pressure. (See the discussion concerning the subroutine ADVECO in the work by Weber *et al.* [1979].) Therefore total energy is not as well conserved as the other global invariants.

The numerical simulation uses a uniform grid of 4465 mesh points with 47 points from $x = 0$ to $x = 1$ and 95 points from $y = 0$ to $y = 2$. This mesh spacing gives a grid resolution of

about 0.02 in each direction, and with this resolution the effective viscous and magnetic Reynolds numbers based on the scale length of the numerical domain are of the order of 10^2 . The overall numerical resolution is relatively poor due to the desire to have the initial filament radius and height as small as possible relative to the size of the numerical box. Having the numerical box large relative to the filament makes it possible to study the initial dynamical evolution of the filament without having to worry about spurious effects introduced by the open boundary conditions.

Typically, the form of SHASTA used in this paper conserves total energy to within an accuracy of 3%, but in some of the runs presented here the total energy increases or decreases by as much as 20%, although typically the error is of the order of 10%. The most important source of error appears to be the low numerical resolution of the sharp magnetic gradients at the current sheet below the current filament. These gradients make it very difficult to compute the energy accurately, and so some of the error in the total energy conservation may come from the trapezoidal rule used to compute the energy rather than from SHASTA.

The computations were carried out using a Prime 9955 and required 509 hours (21.2 days) of CPU time. The Prime 9955 is a mainframe machine with 0.5 million floating point operations per second (mflops) per 5 million integer operations per second (MIPs), and it is comparable to a VAX 8650.

3.2. Numerical Results

Since the initial state within the filament is never in exact equilibrium, flow always appears within the filament almost at once. However, if the initial state starts at a location on the stable branch of the vacuum equilibrium curve of Figure 2, this flow remains small ($v < 0.1$) and does not last very long. As shown in Figures 7 and 8, the initial flow causes the filament's height to decrease about 15% from its initial value. The readjustment of the filament's height is complete by $t = 0.2$, after which time the filament remains stationary until the termination of the simulation at $t = 5.0$ (cf. $M = 2.25$ in Figure 8). Thus the numerical simulation implies that the locations of stable equilibria in the MHD and vacuum models are the same to within 15%. The actual difference

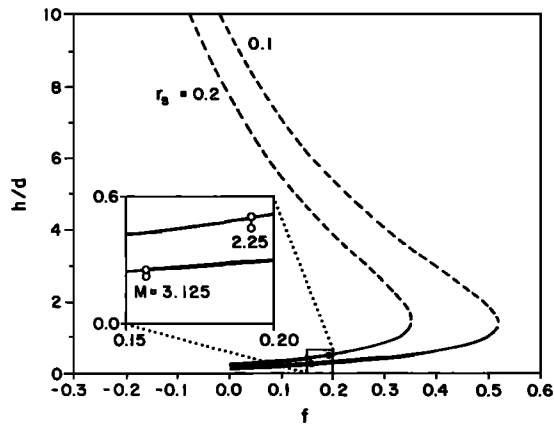


Fig. 7. MHD test of two stable vacuum equilibria configurations (cases 11 and 12). At $t = 0$ the filaments are positioned on the stable equilibrium branch of the vacuum model, but by $t = 5$ the filaments have moved to stable positions slightly below the positions predicted by the vacuum model.

could even be less, since the numerical errors introduced by finite differencing are of this same order (i.e., the ratio of the grid spacing to the initial height, $\Delta x/h_0$, is 16%).

Because of limited computational resources, it was not possible to compute the evolution for more than a dozen different sets of initial conditions (cf. Table 1). The first 10 sets (cases 1–10) all start with the filament at the same height, $h/d = 2.0$, but the strength M of the background field varies in each set. The last two sets (cases 11 and 12) start with the filament's height at $h/d = 0.5$ and $h/d = 0.25$, which are stable equilibria in the vacuum model (cf. Figure 7).

When there is no background field ($M = 0$), the initial repulsive force on the filament is large, and the filament rises rapidly upward, quickly reaching a peak velocity of about 3 times the ambient sound speed. As shown in Figure 8, the filament's trajectory from $t = 0.0$ to $t = 0.2$ is qualitatively similar to the trajectory of a solid cylinder moving in a vacuum (cf. Priest and Forbes [1990]; Steele and Priest [1990]), but after $t = 0.2$ the filament's speed begins to decline. This decline is associated with the development of a strong fast-mode shock wave between $t = 0.2$ and $t = 0.5$. Later on at about $t = 2.0$ the filament's speed begins to

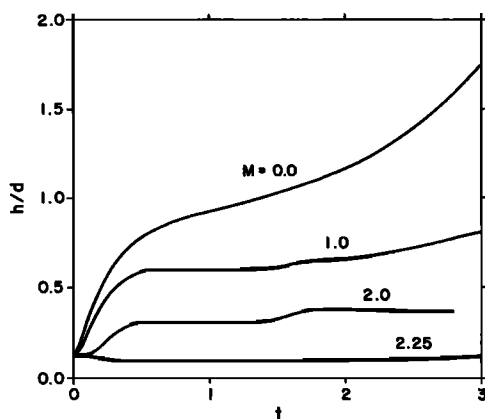


Fig. 8. Filament height h as a function of time. The quantities d and M are the depth and relative strength of the background dipole field.

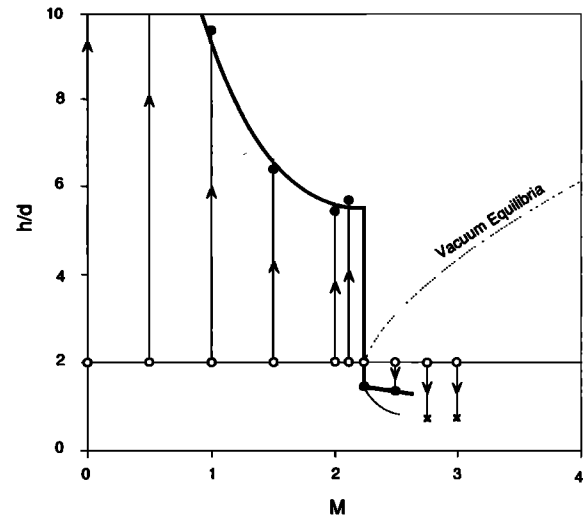


Fig. 9. Final filament height as a function of the relative dipole strength M . Open circles indicate the starting location of the filament at $h/d = 2$, and solid circles indicate the final filament location. The thick solid curve is a freehand interpolation of the numerical results.

increase again, but this increase could be a numerical artifact of the open boundary conditions. By $t = 2.0$ there has been sufficient time for waves propagating outward from the initial disturbance to return to the filament after being reflected from the open boundaries. However, changing the distance between the filament and the open boundaries by a factor of 2 did not produce any appreciable changes in the trajectory, as would be expected if the speed increase was due to wave reflection at the open boundary conditions. An alternate explanation of the speed increase after $t = 2.0$ is that it is due to the very large change in plasma β from the bottom to the top of the box (cf. Figure 6).

When the background magnetic field is present, the initial upward velocity of the filament is reduced, because the initial $\mathbf{j} \times \mathbf{B}$ driving force is weaker. Furthermore, the stretching of the line-tied field lines (cf. Figure 5) creates a tension which slows the upward motion of the filament, and as Figures 8 and 9 show, the tension is sufficient to stop the filament within the numerical domain if $M > 1$. (For $M = 1$ the filament stops at $h/d \approx 0.6$ and then moves downward slightly before continuing to rise further. Since this further rise may be due to boundary condition effects, the first stopping location of the filament is used in Figure 9.)

At $M = 2.19 \pm 0.6$, there appears to be a sudden transition in the height at which the filament stops. As $M = 2.19$ is approached from either side, the filament's stopping height remains constant even though the initial driving force becomes very small. For $M < 2.19$ this constant height is 5.6, while for $M > 2.19$ it is about 1.5, less than the filament's initial height. Thus for $M > 2.19$ the filament actually moves downward rather than upward. The sudden transition from upward to downward motion occurs close to the value of $M = 2.25$ predicted by the vacuum equilibrium model for a filament of radius $0.8d$.

For $M = 2.75$ and $M = 3.0$ the magnetic island which forms the filament disappears as the filament moves downward. In these cases the final equilibrium state consists of closed loops without any o-type or x-type neutral lines. Perhaps this is not too surprising, since the vacuum model

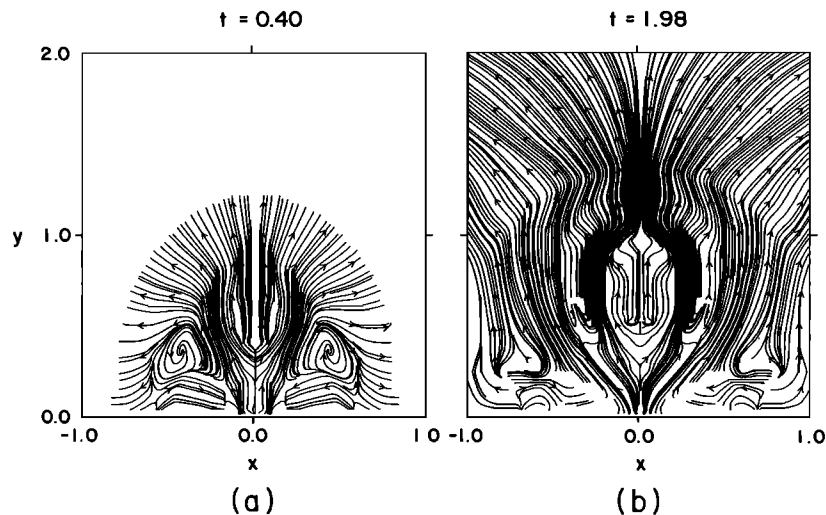


Fig. 10. Velocity streamlines at two different times for the nonequilibrium case with $M = 1.0$ (case 3).

predicts that for $r = 0.8d$ and $M > 2.5$, stable equilibria occur only at locations which require the bottom edge of the filament to be below the base (i.e., $h < r$). Thus severe distortion of the island configuration must occur in the numerical simulation as the filament's height approaches r .

Figure 5 and Plate 1 show the evolution of the magnetic field and the mass density for $M = 1.0$ (case 3). This case corresponds to a nonequilibrium in the vacuum model, so there is already a significant upward force on the current filament at $t = 0$. By $t = 0.2$ a fast shock has formed (the yellow circular arcs in Plate 1), and low-density regions have formed below both the shock and the filament. By $t = 1.60$ the shock has left the numerical box, and only the filament remains. After the shock has left the box, there is a low-density region surrounding the filament, but there is no CME-like shell of dense material which surrounds the filament and moves with it. However, such a shell might develop if the simulation could be run for a longer time or if a stratified density distribution were used initially.

Plate 2 shows the current density at $t = 0.61$ and $t = 1.98$ for the same nonequilibrium case as Plate 1. The current filament is the yellow circular region in the lower central part of each panel, and the fast shock is the thin blue arc above it. The yellow vertical bar projecting upward from the base is the current sheet which forms at the x line. Between the filament and the fast shock there is a slow shock which appears as a red inverted-v-shaped structure in Plate 2. The density jump across this slow shock is so weak that it is just barely perceptible in Plate 1. The density jump is weak because the shock is propagating nearly perpendicular to the magnetic field and because the plasma β upstream of the shock is much greater than 1 [Edmiston and Kennel, 1986]. In the real corona, where β is much less than 1, slow shocks driven by mass ejections can have much stronger density jumps [Steinolfson and Hundhausen, 1989], although for $\gamma = 5/3$ the ratio of downstream to upstream density must still be less than 4 [Ferraro and Plumpton, 1966].

Plate 2 also shows that a weak current layer exists along the open boundaries. This current layer is a numerical artifact which normally has little effect on the dynamics. But if the filament approaches the top boundary, this current layer can become so strong that it disrupts the simulation.

This disruption is the primary reason why it is not possible to determine the long-term evolution for those cases in which the filament exits the numerical domain.

Streamlines at two different times are shown in Figure 10 for the same case as shown in Plates 1 and 2. These streamlines show the velocity field at a particular time, and they do not show the path actually traveled by the fluid elements. At $t = 0.40$ there are vortices on either side of the current sheet, but these vortices do not persist for a very long time at any given location. Instead they propagate outward toward the open boundaries, and by $t = 1.98$ the vortices are no longer within the numerical domain. The slow-mode shock is also visible in Figure 10 as a pronounced rotation of the velocity vectors along an arc just in front of the filament.

Plate 3 shows the divergence and vorticity of the velocity field at $t = 0.61$. The fast shock shows up more clearly in the divergence plot (the red semicircular arc near the top), while the slow shock shows up more clearly in the vorticity plot (the blue inverted-v-structure). In addition to the slow shock, there are strong vorticity features around and below the filament, but the identity of these structures is unknown. Possibly, they are also slow shocks.

In Plate 3 there is rarefaction region which appears in the divergence plot as a pale blue region below the fast shock. This region contains a train of relatively weak cylindrical fast-mode waves which are numerically well resolved, and it is unlikely that this wave train is a computational artifact (i.e., there are normally no spurious oscillations near shocks in SHASTA).

Two effects associated with the boundary conditions are also noticeable in Plate 3. First, the no-slip conditions at the base generate an unresolved shear layer which is evident in the vorticity plot. Second, the open boundary conditions generate an unwanted vorticity just at the point where the fast-mode shock intersects the boundary.

Even though the system of MHD equations used in the simulation are ideal, reconnection still occurs because of the numerical resistivity in the algorithm. The effective numerical resistivity at the x line below the current filament can be determined from Ohm's law by measuring both the current

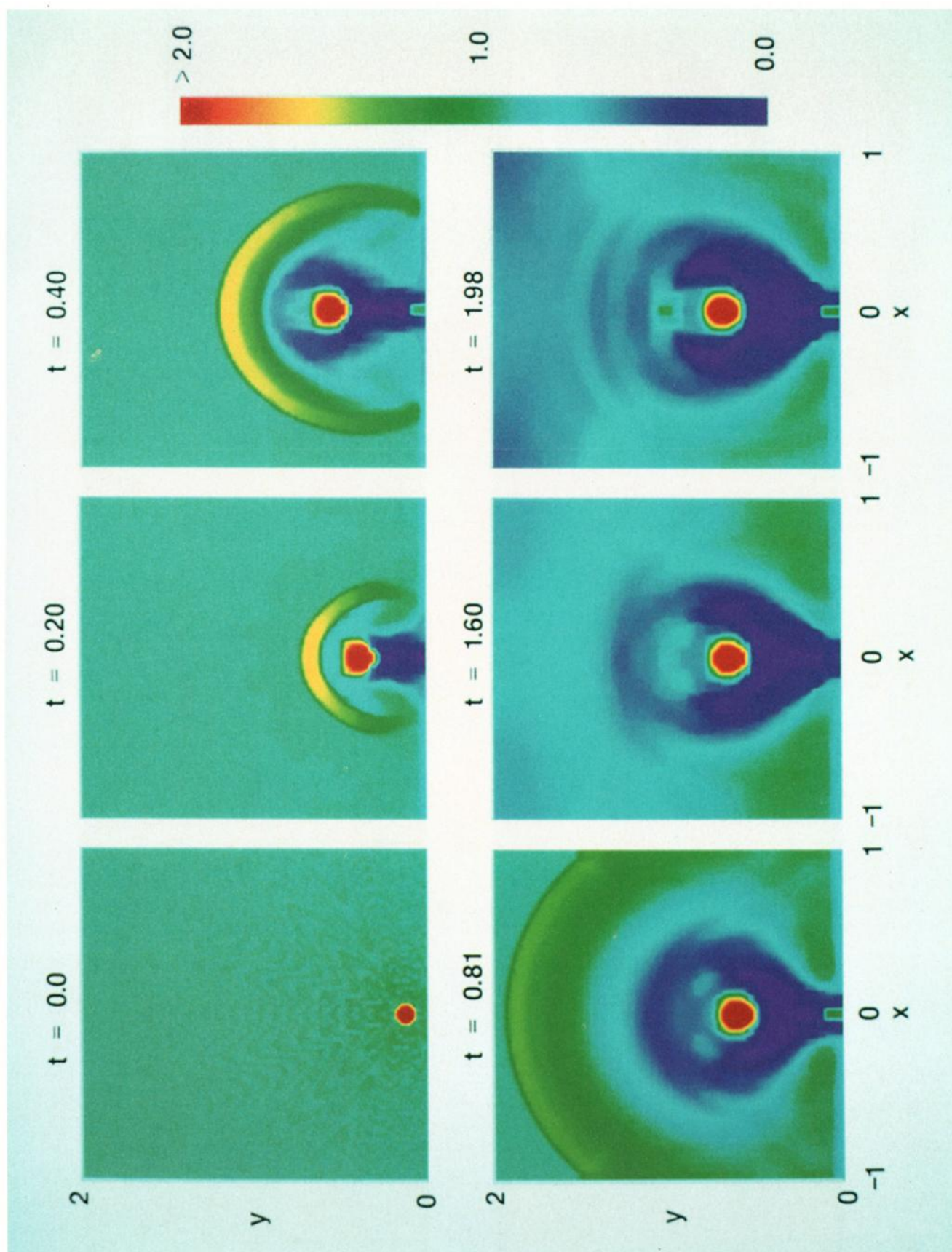


Plate 1. Evolution of the mass density for case 3. The initial state is not an equilibrium one, and so a fast shock (yellow semicircular arc) appears almost at once. By $t = 1.0$ the shock has propagated out of the numerical domain.

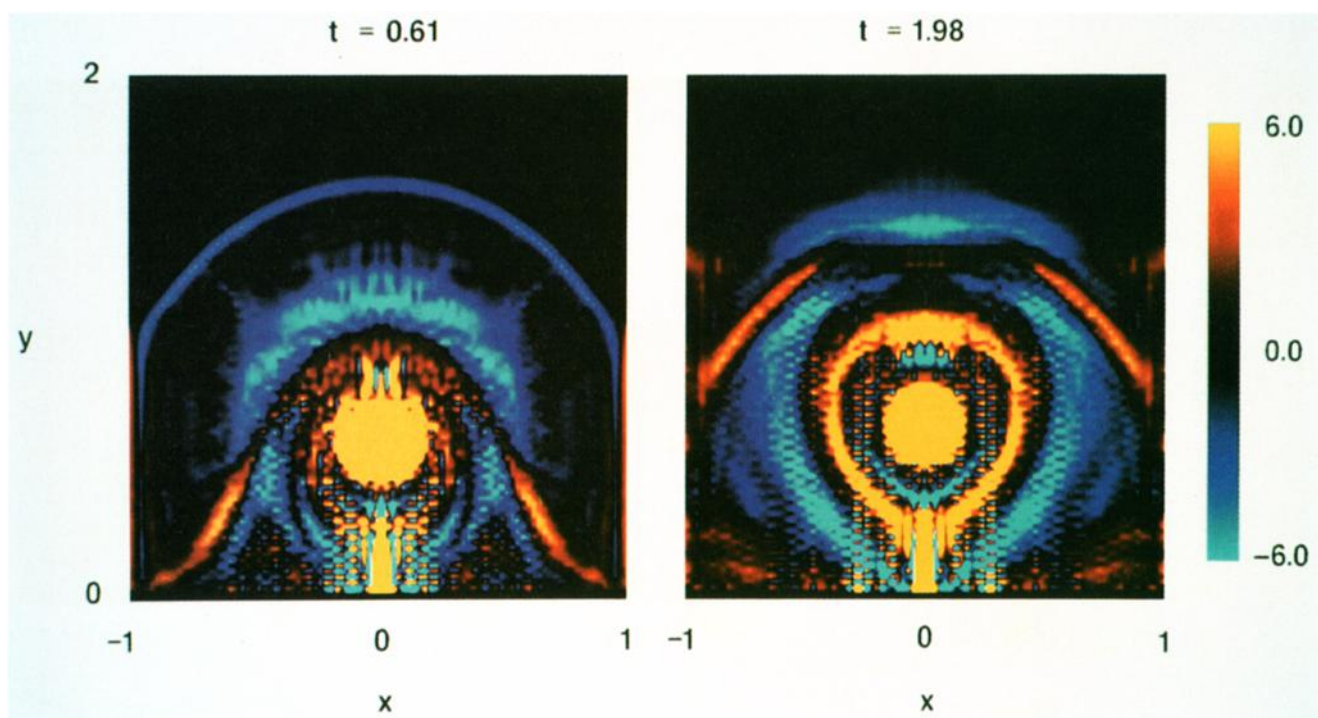


Plate 2. Current density at $t = 0.61$ and $t = 1.98$ for the same case as shown in Plate 1. The speckled pattern in the lower portions of the panels is due to the nonlinear growth of oscillations which have a scale length smaller than the grid resolution [cf. *Matthaeus and Montgomery, 1981*].

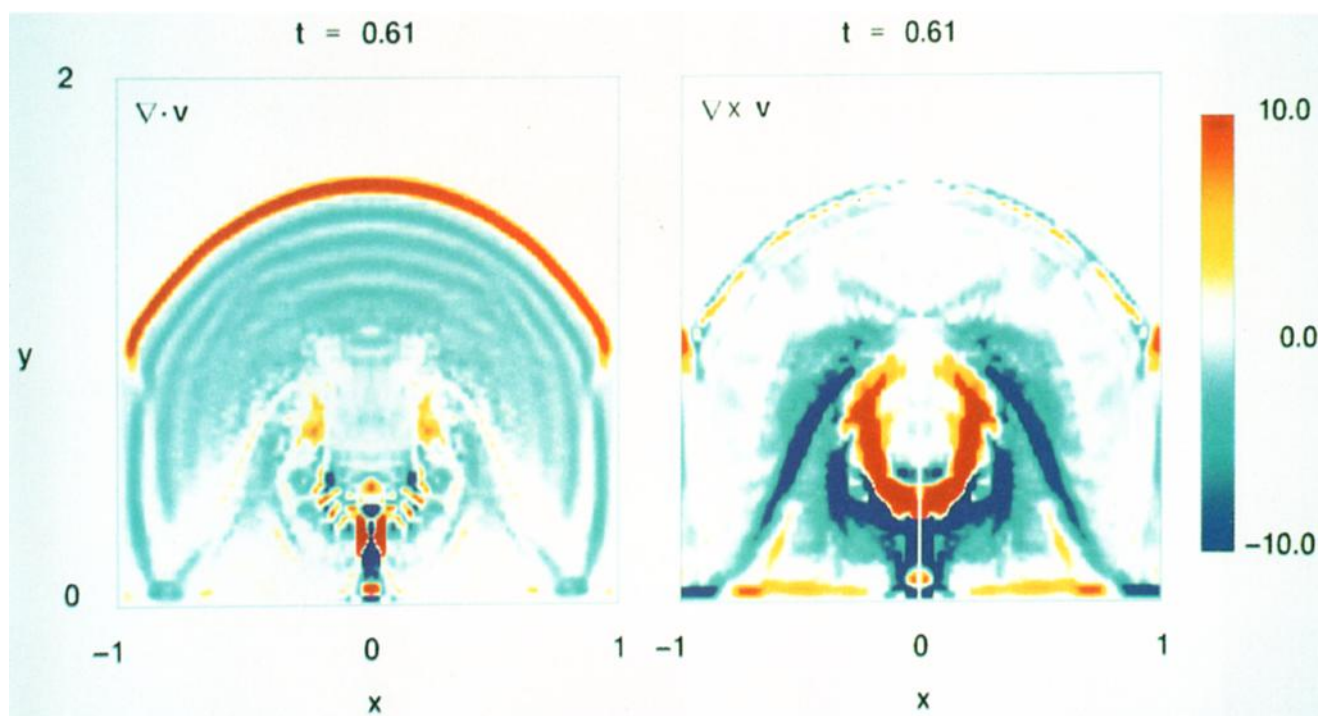


Plate 3. The velocity divergence and vorticity at $t = 0.61$ for the same case as shown in Figure 5 and Plates 1 and 2.

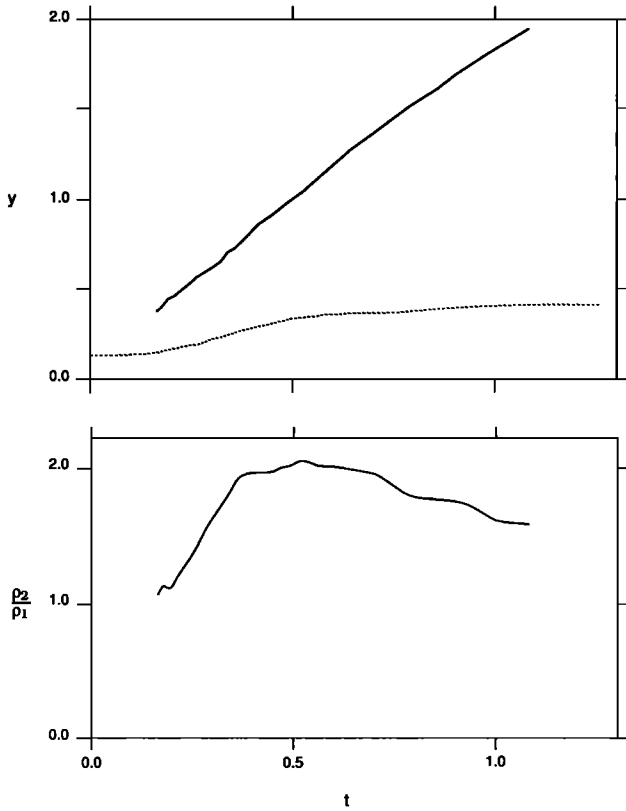


Fig. 11. Fast-mode shock height and strength as a function of time for case 6, which starts very near the unstable branch of the vacuum equilibrium curve. The upper panel shows the shock (solid curve) and filament (dashed curve) heights, while the lower panel shows the shock strength as measured by the ratio p_2/p_1 of upstream to downstream density.

density and the time rate of change of the vector potential at the x line [Forbes, 1988]. That is,

$$\eta_N = -(\partial A / \partial t) / j \quad (36)$$

where η_N , the numerical resistivity in dimensionless units, is just the inverse of the numerical magnetic Reynolds number based on the scale length of the numerical box. For the numerical simulation, η_N is about 1/200, and thus only a small amount of reconnection occurs.

Although the amount of reconnection that occurs during the short time scale of the simulation is relatively small, it is still large enough to produce reconnection jets in the vicinity of the current sheet. In the present simulation, only a single upward directed jet is clearly visible, although short-lived ($\Delta t < 0.1$) bursts of downward flow do occur intermittently. In this simulation the fast-mode Mach number of the reconnection jet never exceeds unity. However, it may be possible to produce a supermagnetosonic reconnection jet by decreasing the initial plasma β and by improving the numerical resolution. If supermagnetosonic outflow from the x line can be achieved, then both upward and downward directed jets should appear [Forbes, 1986; Forbes et al., 1989].

Figure 11 shows the path and strength of the fast shock as a function of time for case 6, where the filament starts at a point very close to the unstable equilibrium branch of the vacuum model (case 6; cf. Figure 2). The initial evolution between $t = 0.0$ and $t = 0.1$ is dominated by the small

readjustment of the field and pressure within the filament due to the lack of a precise equilibrium at $t = 0$. At $t = 0$ the upward $j \times B$ force on the filament is nearly zero, but the developing instability creates a force which pushes the filament upward at an ever increasing rate. The fast shock appears shortly afterward at $t = 0.16$, when the upward motion of the filament (dashed curve) first becomes noticeable in Figure 11. From $t = 0.16$ until $t = 0.5$ the shock's average speed is 1.8 times the ambient sound speed, while the corresponding filament speed is only 0.55, about a third of the shock speed.

The shock strength, as measured by the ratio of downstream to upstream densities, increases rapidly from 1.0 at $t = 0.16$ to about 2.0 at $t = 0.5$, after which time it begins to decline. The decline in shock strength starts at about the same time that the filament's upward rise is halted by the growing tension in the field lines, and the rate of decline is roughly consistent with the damping rate of $r^{-3/4}$ for a cylindrical shock followed by a rarefaction wave [Landau and Lifshitz, 1959, p. 377].

Because total energy is not well conserved (cf. section 3.1), it is difficult to obtain accurate estimates of the magnetic energy conversion occurring in the simulation. Nevertheless, it is still instructive to plot the percentage distribution of the magnetic, kinetic, and internal energies as a function of time. To do this, we first compute the magnetic, kinetic, and internal energies E_m , E_k , and E_i by using the trapezoidal rule to numerically integrate the energy density in the box plus the energy flux through the open boundaries, that is,

$$E_m = \iint \frac{1}{2} B^2 dS + \iint [(-\mathbf{v} \times \mathbf{B}) \times \mathbf{B}] \cdot d\hat{\mathbf{n}} dt \quad (37)$$

$$E_k = \iint \frac{1}{2} \rho v^2 dS + \iint \frac{1}{2} \rho v^2 \mathbf{v} \cdot d\hat{\mathbf{n}} dt \quad (38)$$

$$E_i = \iint (\gamma - 1)^{-1} p dS + \iint \gamma (\gamma - 1)^{-1} p \mathbf{v} \cdot d\hat{\mathbf{n}} dt \quad (39)$$

Dividing E_m , E_k , and E_i by the total energy $E_t (= E_m + E_k + E_i)$ gives the fractional energy distributions f_m , f_k , and f_i at a given time, and the percentage change p in a given form of energy relative to the initial magnetic energy is

$$p = \frac{f - f_0}{f_{m0}} 100\% \quad (40)$$

where f_0 and f_{m0} are the initial values of f and f_m , respectively. Figure 12 plots the relative percentages for the same near-equilibrium case as shown in Figure 11 (case 6). Taken at face value, the figure suggests that about 5% of the total magnetic energy in the box is converted into nearly equal amounts of kinetic and thermal energy.

4. CONCLUSION

The MHD simulation in this paper is based on a catastrophe model proposed by Van Tend and Kuperus [1978] to explain CMEs, flares, and prominence eruptions. Their

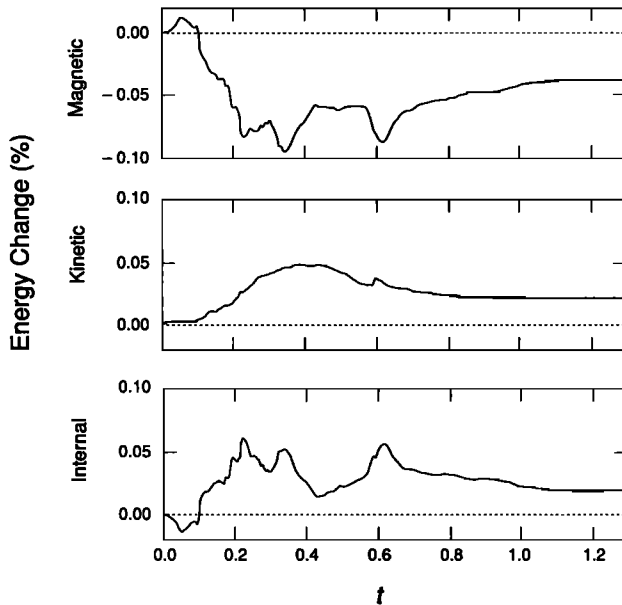


Fig. 12. The evolution of magnetic, kinetic, and internal energy as a function of time for the case which starts very near the unstable branch of the vacuum equilibrium curve (case 6).

model has a current filament which is stable as long as the photospheric magnetic field exceeds a certain critical value, but if the photospheric field is decreased below this critical value, a catastrophic loss of equilibrium occurs. When equilibrium is lost, the filament is magnetically driven upward and away from the Sun.

The ideal MHD simulation implies that in the absence of reconnection the current filament travels upward only a short distance before stopping. Rapid reconnection is needed to relieve the magnetic tension created by the stretching of field lines anchored (i.e., line-tied) to the photosphere. In order for the current filament to continue traveling upward a significant amount of reconnection must occur within a few Alfvén scale times (i.e., a few minutes for typical flare conditions). Whether such rapid reconnection will really occur in the Van Tend and Kuperus model remains to be seen. Recent research suggests that significant reconnection can occur within a few Alfvén scale times if the reconnection is driven by external flows [Priest and Forbes, 1986]. In the Van Tend and Kuperus [1978] model the catastrophic loss of equilibrium may provide such flows, but the ideal simulation in this paper is not suited to answer this question directly. However, the vortical flows downstream of the current filament appear to be promising candidates for rapidly driving the reconnection needed below the filament (cf. Figure 10).

From the point of view of realistically simulating CMEs the simulation is very preliminary, since several important physical effects, such as magnetic reconnection, force-free fields, gravity, and a stratified atmosphere, are not included. In addition to including these effects, future numerical simulations need to achieve a much better numerical resolution and to use more effective open boundary conditions than has been possible here. Unless the reconnection region is well resolved, much of the nonlinear dynamics of the reconnection is suppressed [Steinolfson and Van Hoven,

1984], and unless the simulation can run for long times, it is difficult to determine the reconnection dynamics.

Acknowledgments. The author thanks E. R. Priest and P. Démoulin for their helpful comments, and T. Milliman and R. Anderson for their help with graphics software. This work was supported by NASA grant NAGW-76 and NSF grant ATM-8916303 to the University of New Hampshire.

The Editor thanks J. J. Aly and M. Kuperus for their assistance in evaluating this paper.

REFERENCES

- Aly, J. J., Quasi-static evolution of a force-free magnetic field and the solar flare problem, *Astron. Astrophys.*, **143**, 19, 1985.
- Anzer, U., Can coronal loop transients be driven magnetically?, *Sol. Phys.*, **57**, 111, 1978.
- Birn, J., and K. Schindler, Two-ribbon flares: Magnetostatic equilibria, in *Solar Flare Magnetohydrodynamics*, edited by E. R. Priest, p. 337, Gordon and Breach, New York, 1981.
- Biskamp, D., and H. Welter, Magnetic arcade evolution and instability, *Sol. Phys.*, **120**, 49, 1989.
- Boris, J. P., and D. L. Book, Flux-corrected transport, I, SHASTA, a fluid transport algorithm that works, *J. Comput. Phys.*, **11**, 38, 1973.
- Boris, J. P., and D. L. Book, Flux-corrected transport, III, Minimal-error FCT algorithms, *J. Comput. Phys.*, **20**, 397, 1976.
- Démoulin, P., and E. R. Priest, Instability of a prominence supported in a linear force-free field, *Astron. Astrophys.*, **206**, 336, 1988.
- Edmiston, J. P., and C. F. Kennel, A parametric study of slow shock Rankine-Hugoniot solutions and critical Mach numbers, *J. Geophys. Res.*, **91**, 1361, 1986.
- Ferraro, V. C. A., and C. Plumpton, *An Introduction to Magneto-Fluid Dynamics*, Clarendon, Oxford, 1966.
- Forbes, T. G., Fast-shock formation in line-tied magnetic reconnection models of solar flares, *Astrophys. J.*, **305**, 553, 1986.
- Forbes, T. G., Shocks produced by impulsively driven reconnection, *Sol. Phys.*, **117**, 97, 1988.
- Forbes, T. G., and E. R. Priest, A comparison of analytical and numerical models for steadily driven magnetic reconnection, *Rev. Geophys.*, **25**, 1583, 1987.
- Forbes, T. G., J. M. Malherbe, and E. R. Priest, The formation of flare loops by magnetic reconnection and chromospheric ablation, *Sol. Phys.*, **120**, 285, 1989.
- Gosling, J. T., E. Hildner, R. M. MacQueen, R. H. Munro, A. I. Poland, and C. L. Ross, Mass ejections from the sun: A view from Skylab, *J. Geophys. Res.*, **79**, 4581, 1974.
- Hood, A. W., and Priest, E. R., Kink instability of solar coronal loops as a cause of solar flares, *Sol. Phys.*, **64**, 303, 1979.
- Hundhausen, A. J., The origin and propagation of coronal mass ejections, *Proceedings of the Sixth International Solar Wind Conference, Tech. Note 306 + Proc.*, edited by V. J. Pizzo, T. E. Holzer, and D. G. Sime, p. 181, Natl. Cent. for Atmos. Res., Boulder, Colo., 1988.
- Kaastra, J. J., Solar flares: An electrodynamic model, Ph.D. thesis, Rijksuniversiteit, Utrecht, The Netherlands, 1985.
- Kahler, S., Coronal mass ejections, *Rev. Geophys.*, **25**, 663, 1987.
- Landau, L. D., and E. M. Lifshitz, *Fluid Mechanics*, Pergamon, New York, 1959.
- Linker, J. A., G. Van Hoven, and D. D. Schnack, MHD simulations of coronal mass ejections: Importance of the driving mechanism, *J. Geophys. Res.*, **95**, 4229, 1990.
- Low, B. C., Eruptive solar magnetic fields, *Astrophys. J.*, **251**, 352, 1981.
- Martens, P. C. H., and N. P. M. Kuin, A circuit model for filament eruptions and two ribbon flares, *Sol. Phys.*, **122**, 263, 1989.
- Matthaeus, W. H., and D. Montgomery, Nonlinear evolution of the sheet pinch, *J. Plasma Phys.*, **25**, 11, 1981.
- Mikic, Z., D. C. Barnes, and D. D. Schnack, Dynamical evolution of a solar coronal magnetic field arcade, *Astrophys. J.*, **328**, 830, 1988.
- Mouschovias, T. C., and A. I. Poland, Expansion and broadening of coronal loop transients: A theoretical explanation, *Astrophys. J.*, **220**, 675, 1978.

- Pneuman, G. W., The 'melon-seed' mechanism and coronal transients, *Sol. Phys.*, **94**, 387, 1984.
- Priest, E. R., and T. G. Forbes, New models for fast steady state magnetic reconnection, *J. Geophys. Res.*, **91**, 5579, 1986.
- Priest, E. R., and T. G. Forbes, Magnetic field evolution during prominence eruptions and two-ribbon flares, *Sol. Phys.*, **126**, 319, 1990.
- Reitz, J. R., and Milford, F. J., *Foundations of Electromagnetic Theory*, Addison-Wesley, Reading, Mass., 1960.
- Shibata, K., T. Tajima, R. S. Steinolfson, and R. Matsumoto, Two dimensional magnetohydrodynamic model of emerging magnetic flux in the solar atmosphere, *Astrophys. J.*, **345**, 584, 1989.
- Simmnett, G. M., and R. A. Harrison, The onset of coronal mass ejections, *Sol. Phys.*, **99**, 291, 1985.
- Steele, C. P. C., and E. R. Priest, The eruption of a prominence and coronal mass ejection which drive reconnection, *Sol. Phys.*, **125**, 295, 1990.
- Steinolfson, R. S., Density and white light brightness in looplike coronal mass ejections: Temporal evolution, *J. Geophys. Res.*, **93**, 14,269, 1988.
- Steinolfson, R. S., Driving mechanisms for coronal mass ejections, in *Solar System Plasma Physics, Geophys. Monogr. Ser.*, vol. 54, edited by J. H. Waite, J. L. Burch, and R. L. Moore, p. 269, AGU, Washington, D. C., 1989.
- Steinolfson, R. S., and A. J. Hundhausen, Waves in low- β plasmas: Slow shocks, *J. Geophys. Res.*, **94**, 1222, 1989.
- Steinolfson, R. S., and G. Van Hoven, Nonlinear evolution of the resistive tearing mode, *Phys. Fluids*, **27**, 1207, 1984.
- Steinolfson, R. S., S. T. Wu, M. Dryer, and E. Tandberg-Hanssen, Magnetohydrodynamic models of coronal transients in the meridional plane, 1, The effect of the magnetic field, *Astrophys. J.*, **225**, 259, 1978.
- Sturrock, P. A., Solar flares and magnetic topology, *Sol. Phys.*, **113**, 13, 1987.
- Tousey, R., The solar corona, in *Space Research XIII*, edited by M. J. Rycroft and S. K. Runcorn, p. 713, Akademie, Berlin, 1973.
- van Ballegoijen, A. A., and P. C. H. Martens, Formation and eruption of solar prominences, *Astrophys. J.*, **343**, 971, 1989.
- Van Hoven, G., Simple-loop flares: Magnetic instabilities, in *Solar Flare Magnetohydrodynamics*, edited by E. R. Priest, p. 217, Gordon and Breach, New York, 1981.
- Van Tend, W., The onset of coronal transients, *Sol. Phys.*, **61**, 89, 1979.
- Van Tend, W., and M. Kuperus, The development of coronal electric current systems in active regions and their relation to filaments and flares, *Sol. Phys.*, **59**, 115, 1978.
- Wagner, W. J., SERF studies of mass motions arising in flares, *Adv. Space Res.*, **2**, 203, 1982.
- Wagner, W. J., E. Hildner, L. L. House, C. Sawyer, K. V. Sheridan, and G. A. Dulk, Radio and visible light observations of matter ejected from the sun, *Astrophys. J.*, **244**, L123, 1981.
- Weber, W. J., J. P. Boris, and J. H. Gardener, ALFVEN—A two dimensional code based on SHASTA, solving the radiative, diffusive MHD equations, *Comput. Phys. Commun.*, **16**, 243, 1979.
- Wu, S. T., and J. F. Wang, Numerical tests of a modified full implicit continuous Eulerian (FICE) scheme with projected normal characteristic boundary conditions for MHD flows, *Comput. Methods Appl. Mech. Eng.*, **64**, 267, 1987.
- Wu, S. T., M. Dryer, Y. Nakagawa, and S. M. Han, Magnetohydrodynamics of atmospheric transients, 1, basic results of two-dimensional plane analyses, *Astrophys. J.*, **219**, 324, 1978.
- Yeh, T. Hydromagnetic buoyancy force in the solar atmosphere, *Sol. Phys.*, **95**, 83, 1985.
- Zwingmann, W., Theoretical study of onset conditions for solar eruptive processes, *Sol. Phys.*, **111**, 309, 1987.

T. G. Forbes, Institute for the Study of Earth, Oceans, and Space, University of New Hampshire, Science and Engineering Research Building, Durham, NH 03824.

(Received September 19, 1989;
revised February 7, 1990;
accepted February 9, 1990.)